

Ceramic–metal composites for heat exchangers in concentrated solar power plants

M. Caccia¹, M. Tabandeh–Khorshid¹, G. Itskos¹, A. R. Strayer¹, A. S. Caldwell¹, S. Pidaparti², S. Singnisai¹, A. D. Rohskopf², A. M. Schroeder³, D. Jarrahbashi², T. Kang², S. Sahoo¹, N. R. Kadasala¹, A. Marquez–Rossy⁴, M. H. Anderson³, E. Lara–Curzio⁴, D. Ranjan², A. Henry^{2,5} & K. H. Sandhage^{1*}

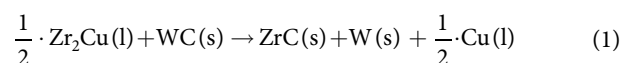
Q1 The efficiency of generating electricity from heat using concentrated solar power plants (which use mirrors or lenses to concentrate sunlight in order to drive heat engines, usually involving turbines) may be appreciably increased by operating with higher turbine inlet temperatures, but this would require improved heat-exchanger materials. By operating turbines with inlet temperatures above 1,023 kelvin using closed-cycle high-pressure supercritical carbon dioxide (sCO₂) recompression cycles, instead of using conventional (such as subcritical steam Rankine) cycles with inlet temperatures below 823 kelvin^{1–3}, the relative heat-to-electricity conversion efficiency may be increased by more than 20 per cent. The resulting reduction in the cost of dispatchable electricity from concentrated solar power plants (coupled with thermal energy storage^{4–6}) would be an important step towards direct competition with fossil-fuel-based plants and a large reduction in greenhouse gas emissions⁷. However, the inlet temperatures of closed-cycle high-pressure sCO₂ turbine systems are limited⁸ by the thermomechanical performance of the compact, metal-alloy-based, printed-circuit-type heat exchangers used to transfer heat to sCO₂. Here we present a robust composite of ceramic (zirconium carbide, ZrC) and the refractory metal tungsten (W) for use in printed-circuit-type heat exchangers at temperatures above 1,023 kelvin⁹. This composite has attractive high-temperature thermal, mechanical and chemical properties and can be processed in a cost-effective manner. We fabricated ZrC/W-based heat-exchanger plates with tunable channel patterns by the shape-and-size-preserving chemical conversion of porous tungsten carbide plates. The dense ZrC/W-based composites exhibited failure strengths of over 350 megapascals at 1,073 kelvin, and thermal conductivity values two to three times greater than for iron- or nickel-based alloys at this temperature. Corrosion resistance to sCO₂ at 1,023 kelvin and 20 megapascals was achieved¹⁰ by bonding a copper layer to the composite surface and adding 50 parts per million carbon monoxide to sCO₂. Techno-economic analyses indicate that ZrC/W-based heat exchangers can strongly outperform nickel-superalloy-based printed-circuit heat exchangers at lower cost.

Q2 If concentrated solar power plants with thermal energy storage were to become cost competitive with fossil-fuel plants for electricity generation, then large-scale penetration of renewable solar energy into the electricity grid^{11–13} would be enabled, resulting in dramatic reductions in man-made CO₂ emissions (we note that the largest sector-level contributor to global greenhouse-gas emissions is the generation of electricity and heat, with electricity accounting for 68 per cent of this sector¹⁴). A major technological barrier inhibiting such competitiveness is the development of compact heat exchangers capable of efficient heat transfer at $\geq 1,023$ K for closed-cycle turbine systems operating with high-pressure sCO₂ power cycles. The maximum stresses that can be sustained by the metal alloys used in printed-circuit heat exchangers decline rapidly above 823 K (for example, allowed stresses fall⁸ to

below 35 MPa at 1,073 K). Heat exchanger materials with enhanced high-temperature failure strength, thermal conductivity, and corrosion resistance that can be cost-effectively manufactured relative to current metal-alloy-based heat exchangers are required.

A key premise of this paper is that composites of ceramics and refractory metals can provide a highly attractive combination of properties for robust, cost-effective, compact heat exchangers⁹ capable of operating at $\geq 1,023$ K and ≥ 20 MPa. We demonstrate this here using co-continuous composites of ZrC and W. These are materials with ultrahigh-melting points (3,695 K for W and up to 3,700 K for ZrC, respectively^{15,16}) that exhibit limited mutual solid solubility, do not react to form other compounds and exhibit a solidus temperature¹⁷ of 3,073 K. Polycrystalline ZrC and W are both thermally conductive^{18,19} ($\alpha = 40 \pm 5$ W·m⁻¹·K⁻¹ and 108 ± 13 W·m⁻¹·K⁻¹, respectively, at 1,000–2,500 K) and exhibit modest values of thermal expansion^{20,21} (0.46% and 0.35%, respectively, from 298–1,023 K). As a result, ZrC/W composites are resistant to thermal shock at high heating rates ($> 1,000$ K·s⁻¹)²². While polycrystalline ZrC is stiff and highly creep resistant²³, polycrystalline W undergoes a brittle-to-ductile transformation²⁴ at ≤ 630 K. Consequently, the carbide phase can endow co-continuous ZrC/W composites with high-temperature stiffness, whereas W can provide high-temperature ductility for enhanced resistance to fracture relative to monolithic ZrC.

Co-continuous ZrC/W composites of the desired shapes (bars, disks, plates) were fabricated via the shape-preserving reactive melt infiltration of rigid, porous tungsten carbide (WC) preforms. The WC preforms were prepared by uniaxial compaction of a WC powder/binder mixture followed by heating to 1,673 K and holding for 2 min under an inert (argon, Ar) atmosphere (to allow for binder removal and initial stage sintering or necking of the WC particles). The resulting $52 \pm 2\%$ porous WC preforms could readily be machined using standard carbide tooling to generate the desired surface features (channels, headers), as shown in Fig. 1a. The porous WC preforms (Fig. 1b and c) were then heated to 1,373 K in a reducing (4% H₂/Ar) atmosphere, lowered into a molten Zr₂Cu bath held at this temperature (and atmosphere) to allow for infiltration, removed from the bulk melt, and then further heated to 1,623 K to promote the following displacement reaction:



The combined volume of the solid reaction products (ZrC and W) is two times larger than the molar volume of the solid reactant (WC)²⁵. Consequently, pores in the rigid WC preforms became filled with the more voluminous solid reaction products, and the non-reactive Cu liquid was forced out, to yield dense ZrC/W-based composites (Fig. 1d–f) that retained the shapes of the starting porous WC preforms (the W particles, along with some unreacted WC, are seen as relatively bright phases, while the ZrC appears as a relatively dark phase in Fig. 1e).

¹School of Materials Engineering, Purdue University, West Lafayette, IN, USA. ²George W. Woodruff School of Mechanical Engineering, Georgia Institute of Technology, Atlanta, GA, USA.

³Department of Engineering Physics, University of Wisconsin, Madison, WI, USA. ⁴Division of Materials Science and Technology, Oak Ridge National Laboratory, Oak Ridge, TN, USA. ⁵Department of Mechanical Engineering, Massachusetts Institute of Technology, Cambridge, MA, USA. *e-mail: sandhage@purdue.edu

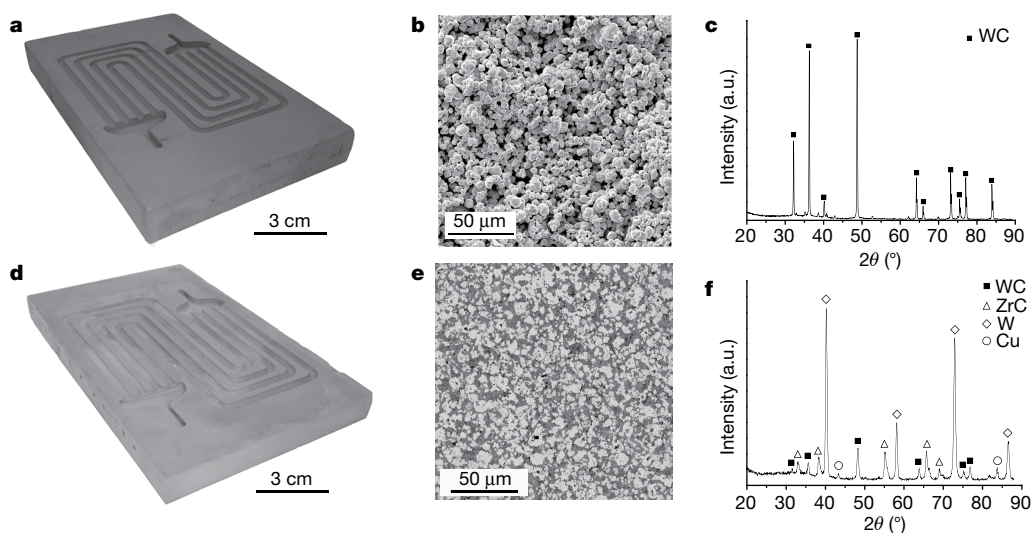


Fig. 1 | Scalable fabrication of dense, channelled ZrC/W plates.

a, Photograph of a porous, rigid WC preform plate with four parallel millichannels in a serpentine pattern with two flat-bottom headers. **b**, **c**, Secondary electron image of a fractured cross-section of a porous, rigid WC preform (**b**) and its corresponding X-ray diffraction pattern (**c**). **d**, Photograph of a dense, channelled ZrC/W-based plate generated by

reactive conversion of a rigid, porous, channelled WC plate.

e, **f**, Backscattered electron image of a polished cross-section of a dense ZrC/W-based composite prepared by reactive Zr₂Cu(l) infiltration into a porous WC preform (**e**) and its corresponding X-ray diffraction pattern (**f**). (a.u., arbitrary units).

Quantitative X-ray diffraction analyses, along with measurements of mass gain upon reactive infiltration, indicated that the ZrC/W-based composites were comprised of 58.1 ± 0.7 vol% ZrC and 35.7 ± 0.4 vol% W, along with residual 2.2 ± 0.6 vol% WC and 4.0 ± 0.7 vol% Cu (average values ± 1 standard deviation, Extended Data Table 1). Comparison of the measured bulk densities ($\rho = 11.15 \pm 0.03$ g·cm⁻³) of these specimens to the theoretical density of this composite ($\rho_{\text{theo}} = 11.43 \pm 0.02$ g·cm⁻³) yielded modest porosity values (<3.0%). Because the reaction-induced increase in solid volume was accommodated by the prior pore volume within the rigid WC preforms, conversion into dense ZrC/W-based composites resulted in average dimensional changes of only $-1.3 \pm 0.8\%$. The shape- and size-preserving nature of this reactive conversion process allows for the cost-effective fabrication of dense, co-continuous ZrC/W composites with well controlled morphologies and dimensions from porous WC preforms that may be readily generated via inexpensive forming operations (which can include stamping and tape casting). Indeed, techno-economic analyses (discussed in more detail in the Methods) indicate that such cost-effective processing can allow channelled ZrC/W-based heat exchanger plates to be manufactured at a cost competitive with or lower than for printed-circuit-type heat exchanger plates comprised of stainless steels or nickel-based superalloys.

The reaction-formed ZrC/W-based composites were found to exhibit attractive thermal and mechanical properties for high-temperature heat exchanger operation. Measurements of the thermal diffusivity²⁶ ($\alpha = 0.201 \pm 0.013$ cm²·s⁻¹) and specific heat capacity ($C_p = 0.285 \pm 0.019$ J·g⁻¹·K⁻¹) of the ZrC/W-based composites yielded an average thermal conductivity ($\kappa = \alpha C_p \rho$) of 66.0 ± 4.6 W·m⁻¹·K⁻¹ at 1,073 K, which was 2.5 to 3 times greater than for Fe-based or Ni-based alloys at this temperature (Extended Data Table 2). The high thermal conductivity of the ZrC/W-based composite relative to Fe-based and Ni-based alloys is of substantial benefit for the performance of compact heat exchangers (that is, higher heat exchanger effectiveness can be achieved for the same heat exchanger geometry). Values of fracture strength were obtained from four-point bend tests^{27,28} at room temperature (298 K) and at 1,073 K in an inert (Ar) atmosphere. The bend tests at 1,073 K were conducted both without and after thermal cycling (ten cycles from room temperature to 1,073 K at a rate of 10 K·min⁻¹). The failure strengths of the ZrC/W specimens obtained at room temperature, at 1,073 K without thermal cycling, and at 1,073 K after thermal cycling

were 348 ± 45 MPa, 369 ± 22 MPa and 387 ± 14 MPa, respectively. The comparable values of failure strength obtained at room temperature and at 1,073 K (with and without thermal cycling) were notable given the dramatic reductions in strength above 823 K reported for metal alloys considered for use in heat exchangers for heat transfer to sCO₂ (that is, maximum allowed working stresses of such metal alloys⁸ are ≤ 35 MPa at 1,073 K). The retained stiffness and strength of the ZrC/W-based composite at 1,073 K allows for the use of thinner heat-exchanger plates comprised of this material than for plates comprised of Fe- or Ni-based alloys which, in turn, can enhance the high-temperature performance and lower the cost of ZrC/W-based heat exchangers.

Another critical issue is oxidation, given that ZrC and W are not oxidation resistant at elevated temperatures^{29,30}. Here we have developed a strategy for endowing ZrC/W-based composites (or other oxidizable materials¹⁰) with resistance to high-temperature oxidation by sCO₂-based fluids. Thermodynamic calculations (discussed in more detail in the Methods) indicated that the addition of >20 parts per million (p.p.m.) CO to sCO₂ will prevent the oxidation of copper according to the following reaction at $\leq 1,073$ K:



where {CO₂} and {CO} refer to carbon dioxide and carbon monoxide, respectively, present in a fluid solution. Hence, Cu should act as an oxidation-resistant surface layer in such supercritical CO/CO₂ mixtures¹⁰. CO/CO₂ mixtures have previously been used to lower the effective oxygen partial pressure in hot CO₂-rich gases at ambient pressure, but the addition of CO to sCO₂-based fluids (for buffered supercritical fluids), coupled with the use of a metal surface layer (such as Cu) that is inert in such fluids¹⁰, has not been previously reported, to our knowledge, as a means of suppressing oxidation in such sCO₂-based fluids. ZrC/W-based composite specimens were sealed within Cu by diffusion bonding, as illustrated in Fig. 2a. Corrosion tests were then conducted for up to 1,000 h at 1,023 K and 20 MPa with sCO₂ fluids containing 50 p.p.m. CO. Weight measurements obtained before and after such exposure from five Cu-encapsulated ZrC/W-converted specimens did not yield a detectable weight gain. A backscattered electron image of a polished specimen cross-section obtained after such exposure, with associated elemental maps for Cu, O, Zr and W, is shown in Fig. 2c. The interface between the Cu layer and ZrC/W-based composite was

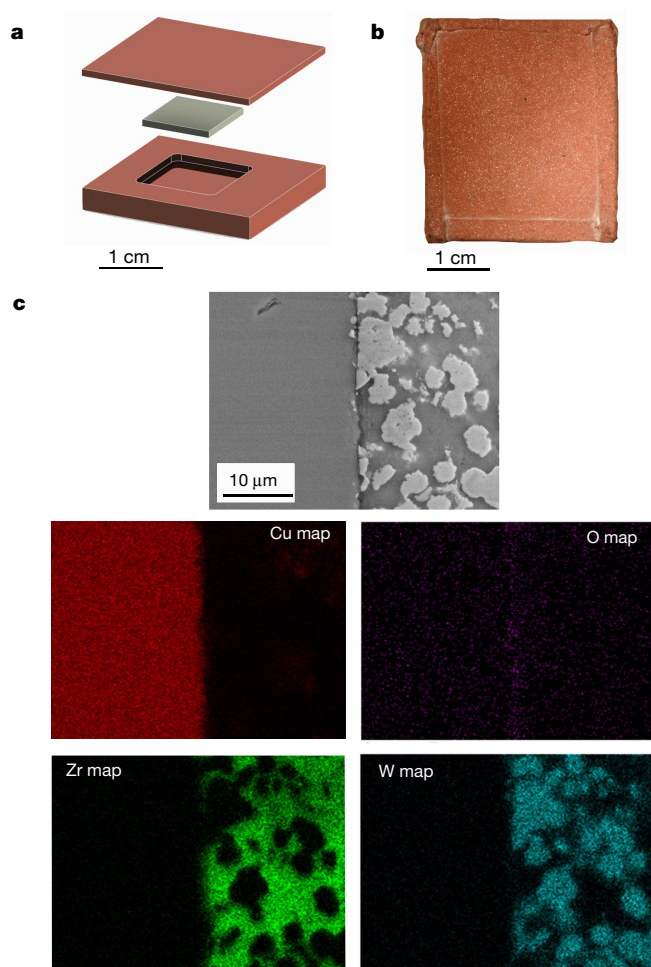


Fig. 2 | Corrosion resistance of a Cu-bearing ZrC/W composite to a buffered supercritical CO/CO₂-bearing fluid at 1,023 K. **a**, Illustration of the Cu encapsulation of a ZrC/W-converted specimen. **b**, Photograph of a Cu-encapsulated ZrC/W specimen after exposure to a sCO₂ fluid containing 50 p.p.m. CO for 1,000 h at 1,023 K and 20 MPa. **c**, Secondary electron image and elemental maps for Cu, O, Zr and W of a polished cross-section of such a specimen, after exposure to a sCO₂ fluid containing 50 p.p.m. CO for 1,000 h at 1,023 K and 20 MPa (the top Cu layer was 1 mm thick).

free of any Zr-O-based or W-O-based scale, which was consistent with the calculated low oxygen flux through Cu from the CO-bearing sCO₂ fluid at 1,023 K (Methods). These tests confirmed that Cu can act as an effective barrier to inhibit corrosion of ZrC/W-based composites (or other oxidizable materials) in buffered supercritical CO/CO₂ fluids.

The appreciably higher values of thermal conductivity and failure strength of ZrC/W composites relative to Fe- or Ni-based structural alloys at $\geq 1,023$ K enables higher values of heat exchanger effectiveness and power density (for the same channel shape, diameter and length). Calculated power density values of a 17.5-MW printed-circuit-type heat exchanger operating with 95% effectiveness for heat transfer to sCO₂ at 873–1,073 K via a Brayton cycle are illustrated in Fig. 3 (see Methods). For these calculations, each printed-circuit-type heat exchanger was assumed to contain channels that were straight and parallel, with semicircular cross-sections of diameter 2 mm and lengths of 2.83 m. The thickness of each plate in the printed-circuit-type heat-exchanger stack and the spacing between the channels (which yielded the volume of solid material and power density) were then determined from the maximum allowed stresses for each type of material (with a factor of safety, FOS, of 2 or 3 considered for the ZrC/W failure bend strength of 370 MPa). As revealed in Fig. 3, the higher values of the strength for ZrC/W-based composites allow printed-circuit-type heat

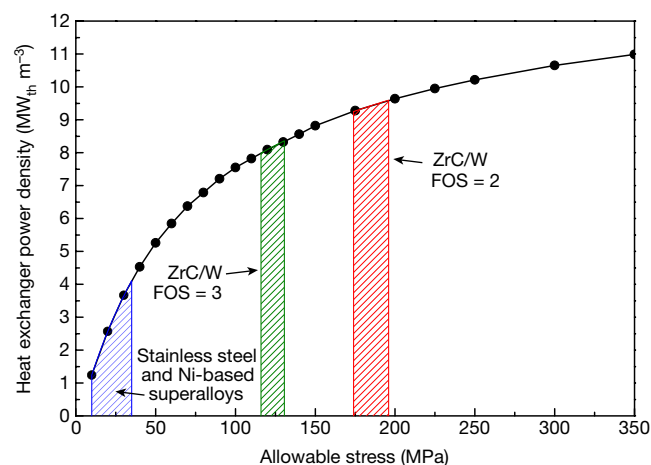


Fig. 3 | The calculated power density of a printed-circuit-type heat exchanger versus allowed stress at 1,073 K. The power density is computed for a 17.5-MW thermal (MW_{th}) heat exchanger with 95% effectiveness for heat transfer to sCO₂ at 873–1,073 K. As the maximum allowable stress of the material increases, thinner plates may be used, which decreases the required solid volume and increases the power density. Dashed regions correspond to the range of maximum allowed stresses for selected metal alloys⁸ (the stainless steels 304 SS and 316 SS and the nickel-based alloys Inconel 617 and 740H) and upper and lower values of failure strengths of ZrC/W-based composites divided by a FOS of 2 or 3.

exchangers to operate at power density values that are at least double those for printed-circuit-type heat exchangers comprised of stainless steels or nickel-based superalloys.

This work demonstrates that cost-effective, reaction-formed composites comprised of co-continuous ceramics and refractory metals, such as ZrC and W, can possess unusual and attractive combinations of properties. The use of such composites in heat exchangers could appreciably enhance the high-temperature performance of renewable concentrated solar power systems, which is an important step towards cost parity with fossil fuel-derived electricity for reduced greenhouse gas emissions. Although in this paper we have focused on compact ZrC/W-based heat exchangers in concentrated solar power systems operating with high-pressure sCO₂-based power cycles at $\geq 1,023$ K, we envisage that cost-effective, reaction-formed ceramic/refractory metal composites could be tailored for use in other desired high-temperature components, enabling more efficient electricity generation in nuclear, natural gas and other power systems.

Online content

Any methods, additional references, Nature Research reporting summaries, source data, statements of data availability and associated accession codes are available at <https://doi.org/10.1038/s41586-018-0593-1>.

Received: 11 June 2018; Accepted: 24 August 2018;

- Dostal, V., Hejzlar, P. & Driscoll, M. J. The supercritical carbon dioxide power cycle: comparison to other advanced power cycles. *Nucl. Technol.* **154**, 283–301 (2006).
- Weinstein, L. E. et al. Concentrating solar power. *Chem. Rev.* **115**, 12797–12838 (2015).
- Irwin, L. & Moullecq, Y. L. Turbines can use CO₂ to cut CO₂. *Science* **356**, 805–806 (2017).
- Pitz-Paal, R. Concentrating solar power: still small but learning fast. *Nat. Energy* **2**, 17095 (2017).
- Lilliestam, J., Labordena, M., Patt, A. & Pfenniger, S. Empirically observed learning rates for concentrating solar power and their responses to regime change. *Nat. Energy* **64**, 17094 (2017).
- Nithyanandam, K. & Pitchumani, R. Cost and performance analysis of concentrating solar power systems with integrated thermal energy storage. *Energy* **64**, 793–810 (2014).
- Williams, J. H. et al. The technology path to deep greenhouse gas emissions cuts by 2050. The pivotal role of electricity. *Science* **335**, 53–59 (2012).

8. American Society of Mechanical Engineers (ASME) *2017 ASME Boiler and Pressure Vessel Code. Section II, Part D Properties (Metric)* <https://www.asme.org/products/codes-standards/bpvcid-2017-bpvc-section-ii-materials-part> (ASME, New York, 2017).
9. Sandhage, K. H. & Henry, A. Methods for manufacturing ceramic and ceramic composite components and components made thereby. International patent application number PCT/US17/28091 (2017).
10. Sandhage, K. H. Method of enhancing corrosion resistance of oxidizable materials and components made therefrom. International patent application number PCT/US17/56015 (2017).
11. Denholm, P. & Maureen, H. Grid flexibility and storage required to achieve very high penetration of variable renewable electricity. *Energy Pol.* **39**, 1817–1830 (2011).
12. Pfenninger, S. et al. Potential for concentrating solar power to provide baseload and dispatchable power. *Nat. Clim. Change* **4**, 689–692 (2014).
13. Denholm, P. & Mehos, M. Enabling greater penetration of solar power via the use of CSP with thermal energy storage. In *Solar Energy: Application, Economics, and Public Perception* (ed. Adaramola, M.), 99–122 (Apple Academic Press, Waretown, 2014).
14. Baumert, K. A., Herzog, T. & Pershing, J. *Navigating the Numbers: Greenhouse Gas Data and International Climate Policy* (World Resources Institute, Washington, 2005).
15. Nagender Naidu, S. V. & Rama Rao, P. *Phase Diagrams of Binary Tungsten Alloys* (ASM International, Materials Park, 1991).
16. Okamoto, H. C-Zr (carbon-zirconium). *J. Phase Equil.* **17**, 162 (1996).
17. Eremenko, V. N., Velikanova, T. Y., Artyukh, L. V., Aksel'rod, G. M. & Vishnevskii, A. S. In *Phase Equilibria Diagrams. Phase Diagrams for Ceramists*. Vol. X. (ed. McHale, A. E.) Fig. 9034 (The American Ceramic Society, Westerville, 1994).
18. Taylor, R. E. Thermal conductivity of zirconium carbide at high temperatures. *J. Am. Ceram. Soc.* **45**, 353–354 (1962).
19. Touloukian, Y. S., Powell, R. W., Ho, C. Y. & Klemens, P. G. *Thermophysical Properties of Matter. Vol. 1. Thermal Conductivity of Metallic Elements and Alloys*. (Plenum Press, New York, 1970).
20. Touloukian, Y. S., Kirby, R. K., Taylor, R. E. & Lee, T. Y. R. *Thermophysical Properties of Matter. Vol. 13. Thermal Expansion of Nonmetallic Solids* (Plenum Press, New York, 1977).
21. Touloukian, Y. S., Kirby, R. K., Taylor, R. E. & Desai, P. D. *Thermophysical Properties of Matter. Vol. 12. Thermal Expansion of Metallic Elements and Alloys* (Plenum Press, New York, 1975).
22. Dickerson, M. B. et al. Near net-shaped, ultra-high melting, recession-resistant ZrC/W-based rocket nozzle liners via the displacive compensation of porosity (DCP) method. *J. Mater. Sci.* **39**, 6005–6015 (2004).
23. Leipold, M. H. & Nielsen, T. H. Mechanical properties of hot-pressed zirconium carbide tested to 2600 °C. *J. Am. Ceram. Soc.* **47**, 419–424 (1964).
24. Lassner, E. & Schubert, W.-D. *Tungsten—Properties, Chemistry, Technology of the Element, Alloys and Chemical Compounds* **22** (Springer, Boston, 1999).
25. Joint Committee on Powder Diffraction Standards (JCPDS) *JCPDS International Center for Diffraction Data File 00–035–0784 for ZrC, 00–025–1047 for WC, 00–004–0806 for W*, <http://www.icdd.com/index.php/pdf-4> (JCPDS International Center for Diffraction Data, Newtown Square, 2007).
26. American Society for Testing and Materials (ASTM) *ASTM Standard Test Method for Thermal Diffusivity by the Flash Method* E1461–13 (ASTM International, West Conshohocken, 2013).
27. American Society for Testing and Materials (ASTM) *Standard Test Method for Flexural Strength of Advanced Ceramics at Ambient Temperature* C1161–18 (ASTM International, West Conshohocken, 2018).
28. American Society for Testing and Materials (ASTM) *Standard Test Method for Flexural Strength of Advanced Ceramics at Elevated Temperatures* C1211–18 (ASTM International, West Conshohocken, 2018).
29. Gasparrini, C., Chater, R. J., Horlait, D., Vandeperre, L. & Lee, W. L. Zirconium carbide oxidation: kinetics and oxygen diffusion through the intermediate layer. *J. Am. Ceram. Soc.* **101**, 2638–2652 (2018).
30. Sikka, V. K. & Rosa, C. J. The oxidation kinetics of tungsten and the determination of oxygen diffusion coefficient in tungsten trioxide. *Corros. Sci.* **20**, 1201–1219 (1980).

Acknowledgements This work was supported by the US Department of Energy, Office of Energy Efficiency and Renewable Energy (award number DE-EE0007117). We thank S. H. Hwang for assistance with electron microscopy and I. Itskou for assistance with the preparation of Cu-encased ZrC/W specimens.

Reviewer information Nature thanks L. F. Cabeza, O. Graeve, C. Turchi and the other anonymous reviewer(s) for their contribution to the peer review of this work.

Author contributions M.C., M.T.-K., G.I. and A.R.S. contributed equally to this work. M.T.-K., A.R.S. and S. Singnisai conducted the WC preform processing and analyses, with assistance from N.R.K. and with K.H.S. providing guidance. M.C. conducted the melt infiltration processing, and analysed the microstructure and chemistry of the resulting ZrC/W composites, with A.R.S., M.T.-K. and A.S.C. providing assistance and with K.H.S. providing guidance. Mechanical tests of ZrC/W composites were conducted and analyzed by S. Sahoo, G.I. and A.M.-R., with E.L.-C. providing guidance. Cu-encased ZrC/W corrosion test specimens were prepared by M.T.-K. Corrosion tests of the Cu-encased ZrC/W specimens were conducted by A.M.S., with M.H.A. providing guidance. Specimen cross-sectional analyses after the corrosion tests were conducted by A.S.C. with assistance from N.R.K. and with K.H.S. providing guidance. Thermodynamic and kinetic calculations associated with corrosion were conducted by K.H.S. Performance calculations of ZrC/W heat exchangers were conducted by S.P., T.K. and D.J., with assistance from K.H.S. and A.H., and with D.R. providing guidance. Economic analyses were conducted by A.D.R., S.P., and A.H., with A.R.S., M.C., G.I. and K.H.S. providing assistance. M.C., G.I., A.H. and K.H.S. drafted the majority of the manuscript. All authors contributed to the writing and review of the manuscript. K.H.S. supervised the overall effort.

Competing interests Authors A.H. and K.S. are inventors on patent applications related to this work that have been filed by (and are owned by) Purdue University and the Georgia Institute of Technology (see refs 10 and 11). Patent application number PCT/US17/28091 includes the fabrication and use of ZrC/W composites for heat exchangers. Patent application PCT/US17/56015 includes enhancement of the high-temperature oxidation resistance of ZrC/W composites through the use of carbon monoxide-bearing supercritical carbon dioxide and a copper surface layer. The other authors declare no competing interests.

Additional information

Extended data is available for this paper at <https://doi.org/10.1038/s41586-018-0593-1>.

Supplementary information is available for this paper at <https://doi.org/10.1038/s41586-018-0593-1>.

Reprints and permissions information is available at <http://www.nature.com/reprints>.

Correspondence and requests for materials should be addressed to K.H.S.

Publisher's note: Springer Nature remains neutral with regard to jurisdictional claims in published maps and institutional affiliations.

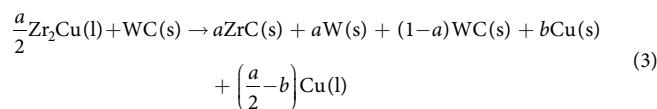
METHODS

Fabrication of rigid, porous WC preforms. Shaped green bodies were generated from mixtures of WC powder (5–6- μm diameter particle size, SC55S, Global Tungsten & Powders) and isobutyl methacrylate (IBMA, Elvacite 2045, Lucite International) as a binder. A slurry comprised of 89 wt% WC powder and an 11 wt% IBMA/acetone solution (11 wt% IBMA dissolved in acetone) was first prepared. The slurry was placed, along with WC milling media (9.5 mm diameter balls; WC ball:slurry weight ratio of 4.4:1), in the tank of a water-cooled attrition mill (SC-1 attritor, Union Process) and then mixed for 10 min with the WC impeller of the attrition mill rotating at 80 r.p.m. After drying for 12 h at room temperature, the resulting solid WC/IBMA powder mixture was milled (ball:powder weight ratio of 4.9:1) for an additional 30 s at 120 r.p.m. (to break up agglomerates) and then passed through a 200 mesh sieve. The WC/IBMA powder mixture (1.4 wt% IBMA) was then formed into plates (9 cm \times 15 cm \times 1 cm) or disks (12.5 mm diameter \times 3 mm thick; 4.85 mm diameter \times 3.8 mm thick) via compaction within single action, graphite-lubricated steel dies of appropriate shape at a peak pressure of 10 MPa at room temperature. The compacted WC/IBMA specimens were then heated in a flowing high-purity Ar atmosphere at 2.5 K $\cdot\text{min}^{-1}$ up to a peak temperature of 1,673 K (to allow for binder removal) and held at this temperature for 2 h (to allow for initial stage sintering or necking of the WC particles) to yield rigid WC preforms with bulk porosity values of 52 \pm 2%. Green machining of the surfaces of rigid, porous WC preforms was conducted with a computer numerical-controlled (CNC) milling machine (Miyano TSV-35, Precision Technologies) at a traverse rate of 38 cm $\cdot\text{min}^{-1}$ using a 3-mm carbide ball tool rotating at 5,000 r.p.m. (to generate channels of semi-circular cross-section) and a flat-bottomed carbide tool (to generate flat-bottomed headers).

Conversion of porous WC preforms into dense ZrC/W composites. The rigid, porous WC preforms were transformed into dense ZrC/W composites via pressureless infiltration and reaction with liquid Zr_2Cu . Alloying of the Zr_2Cu liquid and the reactive melt infiltration process were conducted within a controlled-atmosphere, electrically heated, vertical tube furnace (mullite tube). The Zr_2Cu liquid was prepared by melting stoichiometric mixtures of Zr ($\geq 99.2\%$ purity, Zirconium Research Corp.) and Cu ($\geq 99.9\%$ purity, McMaster Carr) at 1,473 K for ≥ 2 h in a flowing 4% H_2 /Ar atmosphere within a graphite crucible. To allow for immersion and retrieval from the Zr_2Cu liquid bath, the porous WC preform plates or disks were lowered and raised in a vertical orientation within an open graphite support frame consisting of two horizontal plates (a top plate and a bottom plate) and two vertical (side wall) plates. The top horizontal graphite plate contained a hole for connection to a vertical graphite ram (to allow for lowering and raising of the graphite frame containing the porous WC preform into the Zr_2Cu bath). After heating the WC preform and $\text{Zr}_2\text{Cu}(\text{l})$ to 1,373 K (above the 1,273 K congruent melting temperature of Zr_2Cu) in a flowing 4% H_2 /Ar atmosphere, the support frame was lowered at a rate of 5 cm $\cdot\text{min}^{-1}$ into the Zr_2Cu melt bath so as to completely immerse the porous WC preform. After immersion, the infiltrated preform was raised out of the Zr_2Cu melt bath at a rate of 5 cm $\cdot\text{min}^{-1}$ and then heated at 1 K $\cdot\text{min}^{-1}$ to 1,623 K and held at this temperature for 2 h to further the conversion reaction of WC into the ZrC/W composite. After cooling to room temperature within the flowing 4% H_2 /Ar atmosphere, the reacted specimen was removed from the vertical tube furnace.

Macrostructural and microstructural characterization of the ZrC/W composites. Archimedes measurements, using water as the buoyant fluid, were used to obtain density values for the ZrC/W-converted specimens. The overall dimensions and the dimensions of surface features (channels, headers), of the converted specimens were obtained with the use of a digital caliper (CD-6'' CSX ABSOLUTE Digimatic, Mitutoyo) to allow for comparison with the corresponding dimensions of the starting porous WC preform. The ZrC/W-converted specimens were cross-sectioned by a diamond sectioning saw (Techcut 4 Precision Low Speed Saw, Allied High Tech Products Inc.) or by electrodischarge machining (FX20K CNC Wire EDM, Mitsubishi Electric Corp.). Such cross-sections were mounted in epoxy and then ground and polished with a series of diamond pastes to a surface finish of 1 μm . Microstructural analyses of these polished cross-sections were conducted with a field-emission-gun scanning electron microscope (S-4800 FE-SEM, Hitachi) equipped with an energy dispersive X-ray spectrometer (INCA EDS, Oxford Instruments). X-ray diffraction analyses of the phase contents of the ZrC/W-converted specimens were conducted with Cu K α radiation at a scan rate of 3 degrees $\cdot\text{min}^{-1}$ (D2 Phaser diffractometer, Bruker). To allow for quantification of the phase content, X-ray diffraction calibration curves were generated from mixtures of W, WC and ZrC powders combined in proportions consistent with the stoichiometry of reaction (1) for various degrees of reaction.

Quantitative phase analyses of ZrC/W-converted specimens. The reaction of Zr_2Cu liquid within an infiltrated WC preform to form ZrC and W, with residual retained Cu and WC, can be described by the following reaction:



where Cu(s) refers to solid copper retained in the specimen, and Cu(l) refers to liquid copper extruded back out of the specimen (upon filling of the prior pores with the solid ZrC and W products of this reaction). The value of the parameter a for this reaction (an indication of the extent of reaction) is related to the molar W:WC ratio in a reacted specimen as follows:

$$\frac{W}{\text{WC}} = \frac{a}{(1-a)}$$

The molar W:WC ratio was determined from quantitative X-ray diffraction analysis of the reacted specimen; that is, the ratio of the areas A under the (110) and (100) X-ray diffraction peaks for W and WC, respectively, was determined and then a calibration curve (providing the correlation between this $A_{110(\text{W})}/A_{100(\text{WC})}$ ratio and the molar W:WC ratio³¹) was used to determine the molar W:WC ratio. The value of the parameter b was then obtained from the measured mass gain, Δm , of the infiltrated/ reacted specimen, according to the following equation:

$$\frac{\Delta m}{m_0} = \frac{(a\text{MW}_{\text{ZrC}} + a\text{AW}_{\text{W}} + (1-a)\text{MW}_{\text{WC}} + \text{AW}_{\text{Cu}}b) - \text{MW}_{\text{WC}}}{\text{MW}_{\text{WC}}}$$

where m_0 refers to the starting mass of the porous (non-infiltrated) WC preform, MW_i refers to the molecular weight of compound i , and AW_j refers to the atomic weight of element j . Knowledge of parameters a and b , along with the molar volumes^{25,32} of ZrC, WC, W and Cu, were used to determine values of the volume percentages of these phases in reacted specimens. The theoretical densities of non-porous composites comprised of such ZrC, W, WC and Cu mixtures were then compared to measured specimen densities to obtain bulk porosity values. The experimentally determined values of the extent of reaction, phase content, density and porosity for five reactively converted specimens are provided in Extended Data Table 1.

Evaluation of the high-temperature thermal conductivity of ZrC/W composites. A ZrC/W-converted disk was cut by electrodischarge machining into cylindrical specimens with: (1) 12.5 mm diameter and 3 mm thickness (for thermal diffusivity analyses) and (2) 4.85 mm diameter and 3.8 mm thickness (for heat capacity analyses). Laser flash measurements²⁶ (Flashline 4010 Thermal Properties Analyzer, Anter Corporation) were used to obtain thermal diffusivity values, and differential scanning calorimetry (LABSYS Evo TG-DTA-DSC Analyzer, Setaram Instrumentation) was used to evaluate the heat capacity of ZrC/W-converted specimens at 1,073 K (both analyses were conducted at the Orton Materials Testing and Research Center, Westerville, Ohio, USA). These measurements then yielded the value of thermal conductivity at 1,073 K according to the equation $\kappa = \alpha C_p \rho$, with κ the thermal conductivity (in units of $\text{W}\cdot\text{m}^{-1}\cdot\text{K}^{-1}$), α the thermal diffusivity ($\text{cm}^2\cdot\text{s}^{-1}$), ρ the density ($\text{g}\cdot\text{cm}^{-3}$), and C_p the specific heat capacity ($\text{J}\cdot\text{g}^{-1}\cdot\text{K}^{-1}$). The average value of thermal conductivity, and the 95% confidence limit range, were determined from measurements conducted on nine separate specimens.

Evaluation of the fracture strength of ZrC/W composites. A ZrC/W-converted disk was cut by electrodischarge machining into bars of rectangular cross-section, and then ground and chamfered (Bomas Machine Specialties Inc.) to yield four-point bend test specimens with dimensions^{27,28} of 2 mm (± 0.05 mm) \times 1.5 mm (± 0.05 mm) \times 25 mm. Fracture strength tests were conducted at 298 K, at 1,073 K and at 1,073 K after thermal cycling. The latter specimens were cycled ten times between 298 K and 1,073 K at a heating rate of 10 K $\cdot\text{min}^{-1}$ in a high-purity Ar atmosphere. Each test specimen was loaded onto a four-point test fixture (loading span of 20 mm, support span of 10 mm; refs. 27 and 28) contained in a controlled atmosphere furnace. For the tests conducted at 1,073 K, the furnace chamber was evacuated and backfilled three times with 4% H_2 /Ar gas. The temperature was then raised to 1,073 K at a rate of 10 K $\cdot\text{min}^{-1}$ under flowing 4% H_2 /Ar gas. An increasing force was applied with a crosshead speed of 0.0083 mm $\cdot\text{s}^{-1}$, with the force measured continuously to the point of specimen failure. The fracture strength was calculated using the following equation:

$$\sigma_{\text{F}} = \frac{3PL}{4bd^2}$$

with P the break force, L the outer span, b the specimen width and d the specimen thickness. For each of the three test conditions (298 K, 1,073 K and 1,073 K after thermal cycling), the average fracture strength value, and the 95% confidence limit range, were determined from measurements conducted on ten separate specimens.

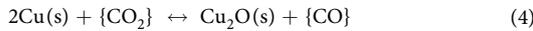
High-temperature thermal and mechanical properties of ZrC/W, IN740H and IN617. Values of the solidus temperature, the high-temperature (1,073 K) specific

Q7

heat capacity, the thermal conductivity and the failure strength for ZrC/W and for the high-temperature nickel-based superalloys, Inconel 740H and Inconel 617, are provided in Extended Data Table 2.

Corrosion resistance of Cu-covered ZrC/W in CO-bearing sCO₂. Corrosion testing of Cu-encased ZrC/W specimens was conducted in a supercritical CO₂ mixture at 1,023 K and 20 MPa. Copper encapsulation was conducted by placing a 10 mm × 10 mm × 1 mm ZrC/W-converted specimen inside a cavity machined into a copper plate (Fig. 2a). A sheet of copper (0.5 mm thick or 1 mm thick) was placed on top of the ZrC/W sample and the copper plate, and hot pressing was then conducted at 1,193 K at 10 MPa for 2 h to bond the copper sheet to the sample and the copper plate. Five such Cu-encapsulated ZrC/W specimens were then exposed to a flowing mixture (around 0.10 kg·h⁻¹) of CO₂ with 50 ± 10 p.p.m. CO (as measured with a gas chromatograph) at 1,023 K and 20 MPa for 1,000 h. Weight change measurements were obtained before and after such exposure for each specimen. The specimens were also cross-sectioned by a diamond sectioning saw, mounted in epoxy, and then polished to a 1-μm finish to allow for analyses with a field-emission-gun scanning electron microscope.

Thermodynamic analysis of Cu compatibility with CO-bearing sCO₂ mixtures at ≤ 1,073 K. Thermodynamic calculations indicated that small additions of CO to the sCO₂ could reduce the oxygen fugacity to values sufficiently low to avoid the oxidation of certain metals, such as copper. Consider the following reaction:



where {CO₂} and {CO} refer to carbon dioxide and carbon monoxide, respectively, present in a fluid solution. For pure Cu and pure stoichiometric Cu₂O present in their pure reference states, the equilibrium CO/CO₂ fugacity ratio for this reaction at 1,073 K and 1 atm total pressure is 15.3×10^{-6} (at 1,023 K, this ratio decreases to 8.12×10^{-6})³³. With equal moles of reactant fluid (CO₂) and product fluid (CO) on both sides of this reaction, the volume *V* change per mole of reaction should be relatively small and is likely to be positive³² (since the volume of one mole of Cu₂O is larger than the volume of 2 moles of Cu). Consequently, the change in the Gibbs free energy for this reaction with total pressure *P* at a given temperature *T* ($\partial\Delta G_{\text{rxn}}/\partial P|_T = \Delta V_{\text{rxn}}$) should be relatively small and probably positive (that is, the equilibrium for this reaction as written above is likely to shift slightly to the left with increasing total pressure), so that the equilibrium CO/CO₂ fugacity ratio for this reaction should probably decrease slightly as the total pressure increases. Hence, with the addition of 20 p.p.m. or more of CO to sCO₂, we expected that the oxidation of Cu in such a CO-bearing sCO₂-based fluid at ≤ 1,073 K and 20 MPa would be avoided¹⁰. This expectation was confirmed by the lack of a detectable weight gain (due to oxidation) of a Cu-encapsulated specimen after exposure to a mixture of 50 p.p.m. CO in sCO₂ for 1,000 h at 1,023 K and 20 MPa.

Analysis of the oxygen flux through Cu. Although the thermodynamic analysis above indicates that Cu should not oxidize in sCO₂ containing 50 p.p.m. CO at ≤ 1,073 K, the low concentration of oxygen present in such a fluid at equilibrium may dissolve into, and migrate through, solid Cu. Hence, a calculation of the maximum oxygen flux through Cu exposed to such a mixture of CO and CO₂ was conducted.

The diffusivity of oxygen *D*_O (in units of cm² s⁻¹) in copper (for temperatures in the range of 973 K to 1,573 K) has been reported to obey the equation³⁴:

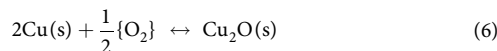
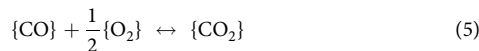
$$D_{\text{O}} = 1.16 \times 10^{-2} \times \exp\{-67,300/R^{-1}T^{-1}\}$$

The solubility of oxygen *X*_O (the oxygen atom fraction) in copper (for the oxygen partial pressure established by the Cu/Cu₂O equilibrium) has been reported to obey the equation³⁴:

$$X_{\text{O}} = 154 \times \exp\{-149,600/R^{-1}T^{-1}\}$$

These equations yield, at 1,023 K, *D*_O = 4.25×10^{-6} cm² s⁻¹ and *X*_O = 3.54×10^{-6} .

The standard Gibbs free energy changes per mole of the following reactions:



at 1,023 K and 1 atm are $\Delta G^{\circ}_{\text{rxn}(5)} = -193,551$ J and $\Delta G^{\circ}_{\text{rxn}(6)} = -93,854$ J (ref. ³³). Hence, the equilibrium oxygen fugacity associated with reaction (5) at a *f*_{CO₂}/*f*_{CO} ratio of 0.99995/0.00005 (50 p.p.m. CO in CO₂) at 1,023 K and 1 atm total pressure is 6.87×10^{-12} atm. The equilibrium oxygen fugacity associated with reaction (6) at 1,023 K and 1 atm total pressure is 2.60×10^{-10} atm. According to Sievert's law³⁵ (which applies for low oxygen contents where Henry's law is valid, as should be the case here for reactions (5) and (6) at 1,023 K), the solubility of a diatomic gas in a condensed phase should vary with the square root of the gas partial pressure}

(or fugacity). Hence the solubility of oxygen in copper that is equilibrated with a 50 p.p.m. CO-bearing sCO₂ mixture at 1,023 K should be (ignoring non-ideal behaviour for the CO-bearing sCO₂ mixture, as an approximation):

$$\begin{aligned} X_{\text{O}}(\text{at fraction for 50 p.p.m. CO/sCO}_2 \text{ equilibrium}) \\ /X_{\text{O}}(\text{at fraction for Cu/Cu}_2\text{O equilibrium}) \\ = \{6.87 \times 10^{-12}/2.60 \times 10^{-10}\}^{1/2} \end{aligned}$$

or

$$\begin{aligned} X_{\text{O}}(\text{at fraction for 50 p.p.m. CO/sCO}_2 \text{ equilibrium}) \\ /3.54 \times 10^{-6} \\ = \{6.87 \times 10^{-12}/2.60 \times 10^{-10}\}^{1/2} \end{aligned}$$

or

$$X_{\text{O}}(\text{at fraction for 50 ppm CO/sCO}_2 \text{ equilibrium}) = 5.75 \times 10^{-7}$$

Consider a dense layer of Cu on top of a ZrC/W composite exposed to such a 50 p.p.m. CO-bearing sCO₂ mixture at 1,023 K. If a linear concentration gradient is assumed for oxygen through the copper layer under steady-state conditions (that is, assuming that the diffusion of oxygen in copper is independent of the oxygen concentration and that chemical reactions at both the CO/sCO₂:Cu and Cu:ZrC/W interfaces are at local equilibrium), then the approximate atomic flux of oxygen *J*_O (in units of moles of oxygen cm⁻² s⁻¹) through such a copper layer may be expressed as:

$$J_{\text{O}} = -D_{\text{O}}\Delta X_{\text{O}}/L\{V_{\text{m}}(\text{Cu})\}$$

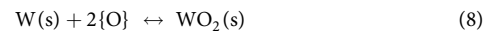
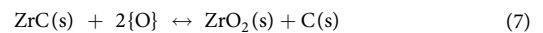
where ΔX_{O} is the difference between the atomic fraction of oxygen dissolved in copper at the Cu:CO/sCO₂ interface and that at the Cu:ZrC/W interface; *L* is the thickness of the copper layer; and *V*_m(Cu) is the molar volume (in units of cm³ per mole) of copper. The maximum flux of oxygen would occur if it is assumed that the mole fraction of oxygen dissolved in Cu at the Cu:ZrC/W interface is zero. Hence, the maximum oxygen flux is given by:

$$J_{\text{O}}^{\text{max}} = -D_{\text{O}}\Delta X_{\text{O}}/L\{V_{\text{m}}(\text{Cu})\}$$

Using a Cu molar volume³² of 7.11 cm³ per mole, along with the values of *D*_O and *X*_O calculated above, the maximum steady-state flux of oxygen through a Cu layer of 1,000 μm (0.1 cm) thickness at 1,023 K in a 50 p.p.m. CO-bearing sCO₂ mixture is thus:

$$J_{\text{O}}^{\text{max}} = -3.44 \times 10^{-12} \text{ moles O cm}^{-2} \text{ s}^{-1}$$

For this value of the oxygen flux, 124×10^{-5} moles of O per cm² (or effectively 6.20×10^{-6} moles of O₂ per cm²) would migrate through such a Cu layer in 1,000 h (3.6×10^6 s). If it is assumed that all of the oxygen arriving at the Cu:ZrC/W interface reacted with ZrC/W to generate either monoclinic ZrO₂(s) or WO₂(s) products by the following reactions, then the corresponding thicknesses of ZrO₂ or WO₂ layers (for ZrO₂ and WO₂ molar volumes of 21.2 cm³ per mole and 19.6 cm³ per mole, respectively³²) would be only 1.3 μm or 1.2 μm, respectively.



Given the assumptions made in this maximum oxygen flux calculation (for example, rapid chemical reactions and local equilibrium at the CO/sCO₂:Cu and Cu:ZrC/W interfaces, complete consumption of all of the oxygen arriving at the Cu:ZrC/W to form ZrO₂ or WO₂, composition-independent diffusion coefficient for oxygen transport through Cu), the modest amount of oxide formation predicted was consistent with the negligible amount of oxide detected at the Cu:ZrC/W interface (Fig. 2) after exposure for 1,000 h to a mixture of 50 p.p.m. CO in sCO₂ at 1,023 K and 20 MPa.

Performance analyses of ZrC/W-based heat exchangers. Performance calculations were conducted for a 17.5 MW-thermal (MW_{th}) counter flow compact (printed-circuit-type) heat exchanger, designed to be representative of an intermediate heat exchanger for a 10 MW-electric (MW_e) concentrated solar power plant. The simulated concentrated solar power plant used a molten KCl–MgCl₂ salt^{36,37} as the thermal energy storage medium and a sCO₂ Brayton cycle for power generation, as depicted in Extended Data Fig. 1.

Thermal-hydraulic design simulations. The operating conditions for the molten salt and sCO₂ in the *Q* = 17.5 MW_{th} intermediate heat exchanger are provided in

Extended Data Table 3. These operating conditions corresponded to a log mean temperature difference (LMTD) of 10 K, for a desired UA value of $1,750 \text{ kW K}^{-1}$ (as in the following equation), and a heat exchanger effectiveness of 95%.

$$Q = UA \times LMTD$$

For the present calculations, it was assumed that the channels in the compact heat exchanger were straight and had a semi-circular cross-section with a diameter (maximum channel width) of 2 mm. The heat exchanger plate width was fixed at 0.60 m. The Reynolds numbers, Re , for the flows of molten salt and $s\text{CO}_2$ were calculated with the assumption that the heat exchanger possessed the same number of channels for both fluids. Published correlations for such compact heat exchangers³⁸ were then used to calculate the overall heat exchanger heat transfer coefficient (U). From the values of UA and U , the total heat transfer area (A) of the heat exchanger was determined. For semi-circular channels of fixed diameter (2 mm), the required heat exchanger area (A) could be achieved with different combinations of the channel length and the number of channels. The values of pressure drop for each fluid, for the operating conditions shown in Extended Data Table 3, were then calculated for various combinations of channel length and channel number³⁸. As an example, the influence of the channel number (for a fixed UA value of 1750 kW K^{-1}) on the pressure drop for each fluid is shown in Extended Data Fig. 2.

Mechanical design calculations. Once the required values of heat transfer coefficient (U), heat exchanger area (A), and associated combinations of channel length and channel number were determined from the thermal-hydraulic design calculations, the total volume of solid material (non-channel volume) in the compact heat exchanger was determined by the pressure containment requirements between the hot and cold streams. The mechanical design calculations were performed to comply with the ASME Boiler and Pressure Vessel Code Section VIII standard for diffusion bonded heat exchangers; that is, the minimum values of the plate thickness and the channel spacing required to stay within certain values of membrane and bending stresses were calculated (Extended Data Fig. 3)³⁹. The values of plate thickness and channel spacing for given allowed stress values (for heat exchangers with straight channels of semi-circular cross-section and a fixed diameter of 2 mm) were then used, along with the desired UA and A values, to determine the total volume (combined solid and channel volumes) of the heat exchanger (in m^3) and the associated value of heat exchanger power density (in $\text{MW}_{\text{th}}\cdot\text{m}^{-3}$). For a variety of stainless steels (such as 304 SS and 316 SS) and nickel-based alloys (such as Inconel 617 and 740H), the maximum allowed stresses at 1,073 K are reported to be in the range⁸ 10–35 MPa. The measured failure strengths of the ZrC/W composites of the present work at 1,073 K were $369 \pm 22 \text{ MPa}$ (with $\pm 22 \text{ MPa}$ referring to the 95% confidence interval range). Assuming an FOS value of 2 to 3 for these ceramic/metal composites (that is, failure strengths of $123 \pm 7 \text{ MPa}$ and $185 \pm 11 \text{ MPa}$, respectively), the calculated values of power density of the ZrC/W-based heat exchangers were found to be a factor of two or more greater than for the metal alloys (Fig. 3) for the operating conditions indicated in Extended Data Table 3.

For example, a power density of $8.2 \text{ MW}_{\text{th}}\cdot\text{m}^{-3}$, and pressure drop values of 100 kPa for $s\text{CO}_2$ and 39 kPa for the molten KCl-MgCl_2 salt, could be achieved with a ZrC/W-based heat exchanger (FOS of 3) with overall dimensions (width \times length \times height) of $0.60 \text{ m} \times 2.83 \text{ m} \times 1.25 \text{ m}$ (comprised of a stack of 804 plates, each of 1.52 mm thickness, with semi-circular channels of 2 mm diameter and centre-to-centre spacing of 2.51 mm, and 182,400 total channels or 91,200 channels for each fluid). For a heat exchanger comprised of Inconel 740H (with a maximum allowed stress^{8,40} of 35 MPa at 1,073 K), such calculations yielded a power density up to $4.1 \text{ MW}_{\text{th}}\cdot\text{m}^{-3}$, with similar pressure drop values, for overall dimensions (width \times length \times height) of $0.60 \text{ m} \times 2.83 \text{ m} \times 2.49 \text{ m}$ (comprised of a stack of 1,215 plates, each of 2.03 mm thickness with semi-circular channels of 2 mm diameter and centre-to-centre spacing of 3.80 mm and 91,200 channels for each fluid). For a heat exchanger comprised of 316 SS (at a maximum allowed stress of 10 MPa at 1073K⁸), such calculations yielded a power density of only up to $1.2 \text{ MW}_{\text{th}}\cdot\text{m}^{-3}$, with similar pressure drop values, for overall dimensions (width \times length \times height) of $0.60 \text{ m} \times 2.83 \text{ m} \times 8.32 \text{ m}$ (comprised of a stack of 2,656 plates, each of 3.12 mm thickness with semi-circular channels of 2 mm diameter and centre-to-centre spacing of 8.30 mm and 91,200 channels for each fluid).

Techno-economic analyses of ZrC/W-based heat exchangers. ZrC/W-based composites were fabricated via the reactive infiltration of WC powder-derived preforms with Zr_2Cu liquid. Direct supplier quotes for bulk quantities of WC, Zr and Cu yielded costs (costs throughout are given in 2018 US dollars) of $\$21.7 \text{ kg}^{-1}$, $\$23.6 \text{ kg}^{-1}$, and $\$6.9 \text{ kg}^{-1}$, respectively, for these raw materials. The combined cost of these starting materials consumed to produce the ZrC/W-based composites was $\$21.8 \text{ kg}^{-1}$, which equates to $\$249,000 \text{ m}^{-3}$ (for a composite theoretical density of $11,430 \text{ kg m}^{-3}$, Extended Data Table 1). The cost of Cu foil (used to coat the ZrC/W composites for resistance to corrosion, Fig. 2) was $\$10 \text{ kg}^{-1}$ (supplier quotes). Hence, the cost of these starting raw materials consumed in the production of a $17.5 \text{ MW}_{\text{th}}$ counter flow compact (printed-circuit-type) ZrC/

W-based heat exchanger with overall dimensions of $0.60 \text{ m} \times 2.83 \text{ m} \times 1.25 \text{ m}$ (width \times length \times height) was $\$0.037 \text{ W}^{-1}$ (for the heat exchanger discussed above, comprised of a stack of 804 plates, each of 1.52 mm thickness, with semi-circular channels of 2 mm diameter and centre-to-centre spacing of 2.51 mm, and with Cu foil used to coat the channels for the $s\text{CO}_2$ -based fluid).

An Excel-based model developed by Ricardo Strategic Consulting for the US Department of Energy was used to evaluate the processing costs (that is, costs associated with producing the final product other than the aforementioned raw material costs). This model utilizes a range of inputs, including the required manufacturing equipment, installation costs, the space and energy needed to operate equipment, the level and associated cost of skilled labour, the time required to process each component, the mean time to failure or replacement of equipment and maintenance costs, indirect costs and other parameters. A conceptual layout was developed for a facility containing the required equipment (for example, for powder/binder mixing, powder compaction, binder removal, preform sintering, preform machining, melt infiltration, diffusion bonding and brazing/welding equipment) necessary to manufacture 100 heat exchanger plates per day (for plates with dimensions of 0.60 m width \times $2.5\text{--}3 \text{ m}$ length \times $1\text{--}2 \text{ mm}$ thickness). After inserting the costs of equipment, labour, energy, maintenance and other inputs into the Ricardo Excel model, it was apparent that the capital equipment expenditure was the dominant processing cost factor. Since the relative contribution of the capital equipment expenditure to the total cost (raw materials + processing) of a given heat exchanger will depend on the rate of production of the heat exchangers (and, in turn, the rate of production of heat exchanger plates), the Ricardo excel model was used to evaluate the heat exchanger plate production rate required for the processing cost to fall well below the cost of raw materials. These calculations indicated that, at a production rate of 10,000 heat exchanger plates per year, the processing cost would fall below 15% of the cost of the raw materials; that is, for a production rate of $>10,000$ plates per year, the total cost of a counter flow compact (printed-circuit-type) ZrC/W-based heat exchanger would be $<\$0.043 \text{ W}^{-1}$ ($<\$25.1 \text{ kg}^{-1}$).

This estimated manufacturing cost for such ZrC/W-based heat exchangers compared favourably to the cost of Ni superalloy-based compact heat exchangers. For example, a compact (printed-circuit-type) heat exchanger comprised of Inconel 740H (IN740H) was considered. The maximum allowed stress^{8,40} of IN740H at 1,073 K is 35 MPa, which allows for a $17.5 \text{ MW}_{\text{th}}$ counter flow compact heat exchanger with a power density of up to $4.1 \text{ MW}_{\text{th}}\cdot\text{m}^{-3}$ (a relatively high value for metal-alloy-based heat exchangers, Fig. 3). This Ni-based alloy contains⁴⁰ 24.5 wt% Cr, 20 wt% Co, 1.5 wt% Nb, 1.35 wt% Al, 1.35 wt% Ti, 0.15 wt% Si, 0.1 wt% Mo and 0.03 wt% C. The commodity prices (<http://www.infomine.com/>) of raw materials for the three major constituents of this alloy ($\$14.6 \text{ kg}^{-1}$ for nickel, $\$4.7 \text{ kg}^{-1}$ for chromium from ferrochrome at $\$2.8 \text{ kg}^{-1}$, $\$91.0 \text{ kg}^{-1}$ for cobalt) yielded a combined raw materials commodity cost of at least $\$26.8 \text{ kg}^{-1}$ for IN740H. The solid volume of IN740H in the $17.5 \text{ MW}_{\text{th}}$ heat exchanger discussed above (with a power density up to $4.1 \text{ MW}_{\text{th}}\cdot\text{m}^{-3}$) with overall dimensions (width \times length \times height) of $0.60 \text{ m} \times 2.83 \text{ m} \times 2.49 \text{ m}$ (comprised of a stack of 1,215 plates, each of 2.03 mm thickness with 91,200 semi-circular channels of 2 mm diameter for each fluid) would be 3.42 m^3 , that is: $[0.6 \text{ m} \times 2.83 \text{ m} \times 2.49 \text{ m}] - [\pi(0.001 \text{ m})^2 \times 2.83 \text{ m} \times 0.5 \times 91,200 \times 2]$. For an IN740H density⁴⁰ of $8,050 \text{ kg m}^{-3}$, such a $17.5 \text{ MW}_{\text{th}}$ IN740H heat exchanger would have mass $2.75 \times 10^4 \text{ kg}$. Hence, the raw materials commodity cost alone of such a $17.5 \text{ MW}_{\text{th}}$ IN740H heat exchanger would be at least $\$0.042 \text{ W}^{-1}$ ($\$26.8 \text{ kg}^{-1} \times 2.75 \times 10^4 \text{ kg} / 17.5 \times 10^6 \text{ W}$). A similar calculation for the four major constituents of IN617 (44.5 wt% Ni, 22 wt% Cr, 12.5 wt% Co, 9 wt% Mo, with smaller amounts of Fe, Al, Mn, Si, Ti, Cu, C, and B), for which the maximum allowed stress^{8,41} at 1,073 K is 32 MPa, yielded a raw materials commodity cost of at least $\$22.4 \text{ kg}^{-1}$ for this alloy (with $\$39 \text{ kg}^{-1}$ for molybdenum from molybdenum trioxide at a commodity cost of $\$26.0 \text{ kg}^{-1}$; <http://www.infomine.com/>), which corresponded to a cost of at least $\$0.037 \text{ W}^{-1}$ ($\$22.4 \text{ kg}^{-1} \times 8,360 \text{ kg m}^{-3} \times 3.42 \text{ m}^3 / 17.5 \times 10^6 \text{ W}$). Hence, comparison of these raw materials commodity costs alone (that is, neglecting the non-trivial processing costs for forming thin plates of these Ni-based alloys, preparing patterned channels into such plates via photochemical etching, and other heat exchanger manufacturing steps) to the manufacturing (raw materials + processing) cost obtained above for compact ZrC/W-based heat exchangers ($<\$0.043 \text{ W}^{-1}$; $<\$25.1 \text{ kg}^{-1}$) indicated that the latter heat exchangers would be comparable in price or less expensive than compact heat exchangers comprised of such high-temperature Ni-based alloys, while achieving twice the power density ($8.2 \text{ MW}_{\text{th}}\cdot\text{m}^{-3}$ versus $4.1 \text{ MW}_{\text{th}}\cdot\text{m}^{-3}$).

The cost of a compact (printed-circuit-type) heat exchanger comprised of 316 SS was also considered. The combined commodity-based cost of the major components of 316 SS ($>62 \text{ wt}\%$ Fe, 17 wt% Cr, 12 wt% Ni, 2.5 wt% Mo) was found to be at least $\$3.6 \text{ kg}^{-1}$ (with $\leq \$0.13 \text{ kg}^{-1}$ for Fe, from iron fines at $\$0.078 \text{ kg}^{-1}$). The solid volume of 316 SS in the $17.5 \text{ MW}_{\text{th}}$ heat exchanger discussed above (with a power density of only up to $1.2 \text{ MW}_{\text{th}}\cdot\text{m}^{-3}$) with overall dimensions (width \times length \times height) of $0.60 \text{ m} \times 2.83 \text{ m} \times 8.32 \text{ m}$ (comprised of a stack of 2,656 plates, each of 3.12 mm thickness

Q8

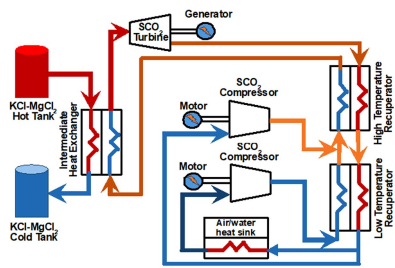
with semi-circular channels of 2 mm diameter and centre-to-centre spacing of 8.30 mm, and 91,200 channels for each fluid) would be 13.3 m³, that is: $[0.6 \text{ m} \times 2.83 \text{ m} \times 8.32 \text{ m}] - [\pi(0.001 \text{ m})^2 \times 2.83 \text{ m} \times 0.5 \times 91,200 \times 2]$. For a 316 SS density of 7,990 kg m⁻³, such a 17.5 MW_{th} IN740H heat exchanger would have mass 1.06×10^5 kg. Hence, the raw materials commodity cost alone of such a 17.5 MW_{th} IN740H heat exchanger would be at least $\$0.022 \text{ W}^{-1}$ ($\$3.6 \text{ kg}^{-1} \times 1.06 \times 10^5 \text{ kg}/17.5 \times 10^6 \text{ W}$).

The photochemical etching cost of 316 SS heat exchanger plates was then considered. Assuming a conservative photochemical etching cost per area of 316 SS of $\$170 \text{ m}^{-2}$ (three times lower than the lowest cost of $\$520 \text{ m}^{-2}$ obtained from vendor quotes for photochemical etching of 2 mm diameter semi-circular channels into 316 SS), the cost of etching 2,656 plates of 2.83 m length and 0.60 m width (total area of plate surfaces to be etched is $4.51 \times 10^3 \text{ m}^2$) for a 17.5 MW_{th} heat exchanger was found to be $\$0.044 \text{ W}^{-1}$ ($\$170 \text{ m}^{-2} \times 4.51 \times 10^3 \text{ m}^2/17.5 \times 10^6 \text{ W}$). Hence, the combined cost estimate (raw materials commodity cost + etching cost) for the 17.5 MW_{th} 316 SS heat exchanger was found to be at least $\$0.066 \text{ W}^{-1}$ (that is, ignoring processing costs other than photochemical etching). Hence, such techno-economic analyses indicated that, for a sufficient manufacturing throughput, compact (printed circuit-type) ZrC/W-based heat exchangers can be manufactured at a lower cost than for state-of-the-art nickel superalloy-based heat exchangers, and at a competitive or lower cost than stainless-steel-based heat exchangers, while achieving at least twice the power density ($8.2 \text{ MW}_{\text{th}} \cdot \text{m}^{-3}$ versus $4.1 \text{ MW}_{\text{th}} \cdot \text{m}^{-3}$ or $1.2 \text{ MW}_{\text{th}} \cdot \text{m}^{-3}$).

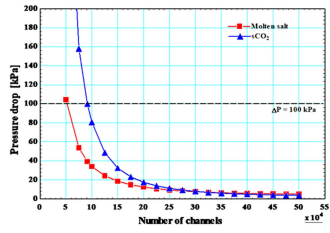
Data availability

Data generated or analysed during this study are available from the corresponding author on reasonable request. Data reported are available within the paper.

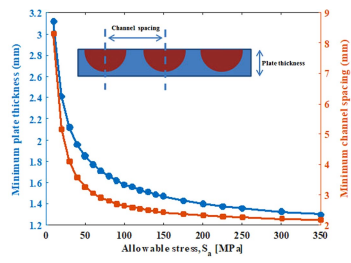
31. Lipke, D. W., Zhang, Y., Liu, Y., Church, B. C. & Sandhage, K. H. Near net shape/net dimension ZrC/W-based composites with complex geometries via rapid prototyping and displacive compensation of porosity (DCP). *J. Eur. Ceram. Soc.* **30**, 2265–2277 (2010).
32. Joint Committee on Powder Diffraction Standards (JCPDS) *JCPDS International Center for Diffraction Data File* 00-004-0836 for Cu, 01-071-3645 for Cu₂O, 00-048-1827 for WO₂ and 01-070-2491 for monoclinic ZrO₂, <http://www.icdd.com/index.php/pdf-4/> (JCPDS International Center for Diffraction Data, Newtown Square, 2007).
33. Barin, I. *Thermochemical Data of Pure Substances* 3rd edn (VCH, Weinheim, 1995).
34. Narula, M. L., Tare, V. B. & Worrell, W. L. Diffusivity and solubility of oxygen in solid copper using potentiostatic and potentiometric techniques. *Metall. Trans. B* **14**, 673–677 (1983).
35. Sieverts, A. The absorption of gases by metals. *Z. Metallk.* **21**, 37–46 (1929).
36. Grijotheim, K., Holm, J. L. & Roetnes, M. Phase diagrams of the systems sodium chloride-magnesium chloride and potassium chloride-magnesium chloride. *Acta Chem. Scand.* **26**, 3802–3803 (1972).
37. Sohal, M. S., Ebner, M. A., Sabharwal, P. & Sharpe, P. *Engineering Database of Liquid Salt Thermophysical and Thermochemical Properties*. Technical Report INL/EXT-10-18297 <https://www.osti.gov/biblio/980801-engineering-database-liquid-salt-thermophysical-thermochemical-properties> (Idaho National Laboratory, Idaho Falls, 2010).
38. Moiseyev, A., Sienicki, J. J., Cho, D. H. & Thomas, M. R. Comparison of heat exchanger modeling with data from CO₂-to-CO₂ printed circuit heat exchanger performance tests. In *Proc. Int. Congress Adv. Nucl. Power Plants (ICAPP) 2010* Paper 2284, 459–468, <http://www.ans.org/store/item-700358/> (American Nuclear Society, La Grange Park, 2010).
39. American Society of Mechanical Engineers (ASME) *2004 ASME Boiler and Pressure Vessel Code. Section VIII, Division 1* NG-3000 (ASME, New York, 2004).
40. Specialty Metals Corp. *Inconel Alloy 740H A Superalloy Specifically Designed For Advanced Ultra Supercritical Power Generation* <http://www.specialmetals.com/assets/smc/documents/alloys/inconel/inconel-alloy-740-h.pdf> (Specialty Metals Corp., New Hartford, 2018).
41. Specialty Metals Corp. *Inconel Alloy 617* <http://www.specialmetals.com/assets/smc/documents/alloys/inconel/inconel-alloy-617.pdf> (Specialty Metals Corp., New Hartford, 2018).



Extended Data Figure 1 | Schematic illustration of a concentrated solar power plant. The thermal energy storage medium is KCl-MgCl₂ molten salt (67% mole%-33 mol%^{36,37}) and the plant uses a sCO₂ Brayton cycle for power generation.



Extended Data Figure 2 | More channels in the heat exchanger reduce the values of pressure drop. Variations of the channel length, and the values of the pressure drop for the molten salt and $s\text{CO}_2$ streams are plotted as a function of the number of channels for each fluid.



Extended Data Figure 3 | Higher allowed stresses reduce the required plate thickness and channel spacing. Values of the minimum plate thickness and minimum channel spacing associated with a given allowed stress are plotted for a compact, printed-circuit-type heat exchanger.

Extended Data Table 1 | Characteristics of the reaction for fabrication of the heat-exchanger plates

Sample Number	W:WC	$\Delta m/m_0$	Reaction Extent*	Phase Content (Vol %)				Density**	Porosity
	(molar ratio)	(%)	(%)	ZrC	W	WC	Cu	[Exptl: Theo] ($g\ cm^{-3}$)	(%)
1	16.4	47.9	94.3	58.1	35.6	2.9	3.4	11.21 : 11.47	2.3
2	15.4	49.9	93.9	56.9	34.9	3.0	5.2	11.14 : 11.43	2.5
3	24.3	49.6	96.0	58.2	35.7	1.9	4.2	11.16 : 11.41	2.2
4	28.3	49.2	96.6	58.7	36.0	1.7	3.6	11.15 : 11.41	2.3
5	29.0	49.3	96.7	58.7	36.0	1.6	3.7	11.11 : 11.41	2.6
Average	22.7	49.2	95.5	58.1	35.7	2.2	4.0	11.15 : 11.43	2.4
S. Deviation	6.4	0.8	1.3	0.7	0.4	0.6	0.7	0.03 : 0.02	0.2

The table shows the values of the molar W:WC ratio (from quantitative X-ray diffraction analysis), mass change upon infiltration, extent of reaction, phase content, density (measured and theoretical) and bulk porosity of five infiltrated and reacted specimens. The standard deviation of the average values are given.

*Reaction extent (%) = $100[(W:WC)/(1 + (W:WC))]$.

**Experimental density values and theoretical (zero porosity) density values (calculated from the indicated phase content for each converted ZrC/W-based specimen) are provided.

Extended Data Table 2 | Material characteristics for ZrC/W, Inconel 740H, and Inconel 617

Material	$T_{\text{solidus}}(K)$	$C_p (J \cdot g^{-1} \cdot K^{-1})$	$\kappa (W \cdot m^{-1} \cdot K^{-1})$	$\sigma_F (MPa)$
ZrC/W	3073 ¹⁷	0.285 [#]	66.0 [#]	369 ^{**}
IN740H	1561 ³³	0.573 ³³	22.1 ³³	56 ^{33*}
IN617	1605 ³⁴	0.611 ³⁴	25.5 ³⁴	54 ^{34***}

The table shows solidus temperatures (T_{solidus}), and average values of the high-temperature (1,073 K) specific heat capacity C_p , thermal conductivity κ and failure strength σ_F . Data are from refs 17, 40 and 41, as indicated.

[#]From the present work.

*Fracture strength.

**Creep rupture stress (100,000 h).

***Creep rupture stress (100,000 h) obtained by interpolation of data at 760 °C and 870 °C.

Extended Data Table 3 | Operating conditions representative of an intermediate heat exchanger for a 10 MW_e concentrated solar power plant

	Molten salt		SCO ₂	
	Pressure (MPa)	Temperature (K)	Pressure (MPa)	Temperature (K)
Inlet	0.1013	1073	20	873
Outlet	-	883	-	1063
Mass flowrate (kg/s)	-	80	-	72.5

The intermediate (primary) heat exchanger is located between the high-temperature fluid heated by sunlight and the supercritical carbon dioxide in the power block, as shown in Extended Data Figure 1. $Q = 17.5 \text{ MW}_{\text{th}}$ for this molten-salt-to-SCO₂ compact heat exchanger.

Q9